

OPTICAL-UV SPECTRUM AND PROPER MOTION OF THE MIDDLE-AGED PULSAR B1055–52

R. P. MIGNANI¹, G. G. PAVLOV², O. KARGALTSEV³

Draft version July 24, 2018

ABSTRACT

PSR B1055–52 is a middle-aged ($\tau = 535$ kyr) radio, X-ray, and γ -ray pulsar showing X-ray thermal emission from the neutron star (NS) surface. A candidate optical counterpart to PSR B1055–52 was proposed by Mignani and coworkers based on *Hubble Space Telescope* (*HST*) observations performed in 1996, in one spectral band only. We report on *HST* observations of this field carried out in 2008, in four spectral bands. The astrometric and photometric analyses of these data confirm the identification of the proposed candidate as the pulsar’s optical counterpart. Similarly to other middle-aged pulsars, its optical-UV spectrum can be described by the sum of a power-law (PL_O) component ($F_\nu \propto \nu^{-\alpha_O}$), presumably emitted from the pulsar magnetosphere, and a Rayleigh-Jeans (RJ) component emitted from the NS surface. The spectral index of the PL_O component, $\alpha_O = 1.05 \pm 0.34$, is larger than for other pulsars with optical counterparts. The RJ component, with the brightness temperature $T_O = (0.66 \pm 0.10) d_{350}^2 R_{O,13}^{-2}$ MK (where d_{350} and $R_{O,13}$ are the distance to the pulsar in units of 350 pc and the radius of the emitting area in units of 13 km), shows a factor of 4 excess with respect to the extrapolation of the X-ray thermal component into the UV-optical. This hints that the RJ component is emitted from a larger, colder area, and suggests that the distance to the pulsar is smaller than previously thought. From the absolute astrometry of the *HST* images we measured the pulsar coordinates with a position accuracy of $0''.15$. From the comparison with previous observations we measured the pulsar proper motion, $\mu = 42 \pm 5$ mas yr^{−1}, which corresponds to a transverse velocity $V_t = (70 \pm 8) d_{350}$ km s^{−1}.

Subject headings: pulsars: individual (PSR B1055–52) — stars: neutron

1. INTRODUCTION

The radio pulsar B1055–52 (also known as PSR J1057–5226) was discovered by Vaughan & Large (1972). The period, $P = 197$ ms, and its derivative, $\dot{P} = 5.83 \times 10^{-15}$ s s^{−1}, correspond to the spin-down age $\tau = P/2\dot{P} = 535$ kyr, rotational energy loss rate (spin-down power) $\dot{E} = 3.0 \times 10^{34}$ erg s^{−1}, and surface magnetic field $B = 1.1 \times 10^{12}$ G. Neither proper motion nor parallax measurements have been reported for this pulsar so far. Based on the pulsar’s dispersion measure, DM=30.1 pc cm^{−3}, the distance was estimated as $d = 1.53$ kpc for the Galactic free electron density model by Taylor & Cordes (1993), while the NE2001 model by Cordes & Lazio (2002) yields $d = 0.73 \pm 0.15$ kpc.

PSR B1055–52 was one of the few radio pulsars detected by the *Einstein* X-ray observatory (Cheng & Helfand 1983). Observations with *EXOSAT* showed a thermal nature of its soft X-ray emission, presumably originating from the neutron star (NS) surface (Brinkmann & Ögelman 1987), while *ROSAT* observations found that at least two spectral components were needed to fit the spectrum (e.g., a blackbody [BB] and a power-law [PL]) and discovered X-ray pulsations at the radio period (Ögelman & Finley 1993). The similarities

in the ages and X-ray properties with two nearby middle-aged pulsars, PSR B0656+14 ($\tau = 110$ kyr) and Geminga ($\tau = 340$ kyr), for which *ROSAT* also detected thermal X-ray emission, earned these three pulsars the nickname of “The Three Musketeers” (Becker & Trümper 1997).

The X-ray spectrum and pulsations of PSR B1055–52 were also studied with *ASCA* (Greiveldinger et al. 1996; Wang et al. 1998) and *BeppoSAX* (Mineo et al. 2002). Recent observation with the more sensitive *Chandra* (Pavlov et al. 2002) and *XMM-Newton* (De Luca et al. 2005) have shown that the phase-integrated X-ray spectrum, similar to those of the other two “Musketeers”, can be fitted with three spectral components: a cold BB ($T_C \approx 0.8$ MK), a hot BB ($T_H \approx 1.8$ MK), and a PL component (photon index $\Gamma \approx 1.7$, luminosity $L_X^{\text{nonth}} \sim 8 \times 10^{30} d_{750}^2$ erg s^{−1} in the 0.5–10 keV band, where $d_{750} = d/(750 \text{ pc})$), presumably emitted from the pulsar magnetosphere. Phase-resolved spectroscopy of the *Chandra* and *XMM-Newton* data suggests that the changing projected emitting area of the hot component is responsible for the bulk of the phase variations (Pavlov et al. 2002; de Luca et al. 2005).

PSR B1055–52 was one of the seven γ -ray pulsars detected by the EGRET instrument aboard the *Compton Gamma-ray Observatory* (*CGRO*) (Fierro et al. 1993; Thompson et al. 1996). It has also been studied by the *Fermi* LAT detector (Abdo et al. 2010). Its 0.1–100 GeV luminosity, $L_\gamma \sim 2 \times 10^{34} d_{750}^2$ erg s^{−1} (assuming an approximately isotropic emission), implies an extremely high γ -ray efficiency, $\eta_\gamma \equiv L_\gamma/\dot{E} \sim 0.6 d_{750}^2$.

To study and interpret the magnetospheric and thermal emission from PSR B1055–52, the X-ray and γ -ray

¹ Mullard Space Science Laboratory, University College London, Holmbury St. Mary, Dorking, Surrey, RH5 6NT, UK; rm2@mssl.ucl.ac.uk

² Department of Astronomy and Astrophysics, Pennsylvania State University, PA 16802, USA; pavlov@astro.psu.edu

³ Department of Astronomy, University of Florida, FL 32611, USA; oyk100@astro.ufl.edu

data should be supplemented by optical data. However, optical observations with ground-based telescopes (Manchester et al. 1978; Cheng & Helfand 1983; Big-nami et al. 1988) failed to detect PSR B1055–52 because of the presence of a bright ($V \approx 14$) F-type field star $\approx 4''$ from the radio pulsar position (dubbed Star A by Manchester et al. 1978). Thanks to the sharp resolution and high sensitivity of the Faint Object Camera (FOC) aboard the *Hubble Space Telescope* (*HST*), Mignani et al. (1997; hereafter M+97) were able to identify a faint ($U \sim 25$) probable counterpart at the radio pulsar position. Since the observation was taken in only one filter, the shape of the optical spectrum of the candidate counterpart remained unknown, and even its identification with the pulsar was not certain. To confirm the identification, measure the spectral shape (in particular, separate the magnetospheric and thermal components, similar to the two other Musketeers – see, e.g. Kargaltsev & Pavlov 2007; KP07 hereafter), and measure the optical pulsations, new *HST* observations were obviously required. Our proposal to reobserve PSR B1055–52 with *HST* was accepted for Cycle 16 (program 11154). These observations are described in Section 2, while the results are presented in Section 3, discussed in Section 4, and summarized in Section 5.

2. OBSERVATIONS AND DATA ANALYSIS

As no timing capabilities were available in the *HST* Cycle 16, we could only image the target in several filters. To observe PSR B1055–52 in the far-UV (FUV), most useful for studying the thermal component, we employed the Solar Blind Channel (SBC) detector of the Advanced Camera for Surveys (ACS). The SBC is a CsI Multi-Anode Microchannel Array (MAMA) photon-counting detector, which is operated in ACCUM mode producing time-integrated images. The detector is sensitive to radiation in the 1115–1700 Å wavelength range, and it provides a nominal field of view (FOV) of $34''.6 \times 30''.1$, with a pixel scale of $0''.034 \times 0''.030$. To filter out the geocoronal lines, we used the longpass filter F140LP (pivot wavelength $\lambda = 1528$ Å; equivalent gaussian FWHM $\Delta\lambda = 297$ Å), which cuts off radiation at $\lambda \lesssim 1350$ Å. The pulsar was observed on 2008 February 13 over two consecutive spacecraft orbits for a total integration time of 5569 s. The data were reduced and calibrated (including the linearity correction, dark subtraction, flat-fielding) through the ACS data reduction pipeline (CALACS), using the closest-in-time calibration frames. Geometric distortion correction, cosmic-ray filtering, and exposure stacking were applied during the pipeline processing using the `MultiDrizzle` task. This task also applied a re-sampling of the drizzled image to an even pixel size of $0''.025$.

We also observed PSR B1055–52 in three optical bands with the Wide Field and Planetary Camera 2 (WFPC2)⁴ on 2008 March 8. To exploit the maximum spatial resolution, the pulsar was centred in the Planetary Camera (PC) chip, which has a pixel scale of $0''.045$ and a FOV of $35'' \times 35''$. To maximize the spectral coverage, we observed through the F450W ($\lambda = 4557$ Å; $\Delta\lambda = 951$

Å), F555W ($\lambda = 5442$ Å; $\Delta\lambda = 1229$ Å), and F702W ($\lambda = 6917$ Å; $\Delta\lambda = 1381$ Å) filters. Observations were carried out during four consecutive orbits for the total integration times of 3600 s in the F450W filter and 1800 s in each of the F555W and F702W filters. For each filter, the observations were split in shorter, dithered exposures of 600 s to filter out cosmic ray hits and bad pixels. The data were processed through the WFPC2 CALWP2 reduction pipeline for bias, dark, and flat-field correction and flux calibration. For each filter, we then combined single exposures with the IRAF task `drizzle` to produce co-added and cosmic-ray-free images.

We also used the archival FOC observations by M+97. They were carried out on 1996 May 11 in the F342W filter ($\lambda = 3402$ Å; $\Delta\lambda = 519$ Å) during three spacecraft orbits with the exposure times of 2771 s for the first orbit and 3062 s for the second and third orbits, corresponding to the total integration time of 8895 s. The data were obtained with the high-resolution F/96 relay, with the FOV of $7'' \times 7''$ and pixel scale of $0''.014$. The data were retrieved from the *HST* science data archive⁵ and on-the-fly recalibrated through the CALFOC reduction pipeline with the updated reference files.

3. RESULTS

3.1. Detection of the candidate counterpart

The most recent published radio coordinates of PSR B1055–52 (Newton et al. 1981),

$$\alpha = 10^{\text{h}}57^{\text{m}}58^{\text{s}}84 \pm 0^{\text{s}}.03, \quad \delta = -52^{\circ}26'56''.3 \pm 0''.3, \quad (1)$$

are for the epoch of 1978.13 (equinox J2000). These coordinates, without proper motion values, are reported in the ATNF radio pulsar catalogue⁶ (Manchester et al. 2005), and they were also used by Weltevrede et al. (2010) to compute the PSR B1055–52 radio ephemeris for the timing of the *Fermi* γ -ray observations. Since pulsars are known to have high velocities, PSR B1055–52 could move a few arcseconds in the 30 year span between the epochs of the radio position and our *HST* observations (2008.12 and 2008.18). For instance, for an average radio pulsar velocity of 400 km s⁻¹ (e.g., Hobbs et al. 2005), we would expect a proper motion of $110 d_{750}^{-1}$ mas yr⁻¹ and a position shift of $3''.4 d_{750}^{-1}$ in 30 years, in an unknown direction. Such an uncertainty hampers a direct identification based on the pulsar’s position only. Fortunately, the presence of Star A in the immediate vicinity of the pulsar can be used for the pulsar identification.

The $10'' \times 10''$ cutout of the SBC image of the PSR B1055–52 field (left panel of Figure 1) shows the only two objects detected in the entire SBC FOV, separated by a distance of $4''.41$. From the comparison of this image with that obtained by M+97 with FOC, it is natural to assume that the northwestern and southeastern objects are Star A and the candidate pulsar counterpart, respectively.

Indeed, the nominal SBC coordinates of the northwestern source are $\alpha = 10^{\text{h}}57^{\text{m}}58^{\text{s}}790$ and $\delta = -52^{\circ}26'53''.04$. The most accurate coordinates of Star A, $\alpha_A =$

⁴ We originally proposed the observations in the optical bands for the higher throughput ACS Wide Field Channel (WFC), but we had to switch to the WFPC2 since the WFC was turned off in January 2007 because of problems with the ACS electronics.

⁵ See <http://archive.stsci.edu>.

⁶ See <http://www.atnf.csiro.au/research/pulsar/psrcat/>.

$10^{\text{h}}57^{\text{m}}58^{\text{s}}.728 \pm 0^{\text{s}}.004$ and $\delta_A = -52^{\circ}26'52''.45 \pm 0''.06$, at the epoch of our *HST* observation, can be derived from the Third US Naval Observatory CCD Astrograph Catalog (UCAC3; Zacharias et al. 2010), with account for the Star A’s proper motion, $\mu_\alpha = -8.9 \pm 1.3 \text{ mas yr}^{-1}$ and $\mu_\delta = 7.8 \pm 2.2 \text{ mas yr}^{-1}$, given in the same catalog and independently verified by us (see Appendix). As the difference between these and the nominal SBC coordinates ($0''.57$ and $-0''.59$ in right ascension and declination, respectively) is within the error budget of the *HST* absolute astrometry, we conclude that the SBC northwestern source is indeed Star A.

Applying the boresight correction to the SBC image, such that the coordinates of the northwestern source coincide with the UCAC3 coordinates of Star A, we obtain the following coordinates of the southeastern source

$$\alpha = 10^{\text{h}}57^{\text{m}}58^{\text{s}}.954, \quad \delta = -52^{\circ}26'56''.37, \quad (2)$$

with a nominal position uncertainty of about $0''.07$. This uncertainty is mostly determined by the uncertainty of the UCAC3 absolute astrometry, thanks to the small angular distance ($4''.41$) between Star A and PSR B1055–52, and the $\sim 0.1^\circ$ accuracy on the *HST* roll angle with respect to the equatorial reference frame.

The derived position is consistent with the candidate pulsar counterpart position in the FOC observation ($\alpha = 10^{\text{h}}57^{\text{m}}58^{\text{s}}.832$, $\delta = -52^{\circ}26'56''.28$), within the uncertainty of the FOC position ($\approx 1''.0$)⁷ and the uncertainty caused by an unknown proper motion since the epoch of the FOC observation (1996.36). This suggests that we indeed detected the PSR B1055–52 candidate counterpart of M+97 in our SBC image, while the extremely blue color (obvious from the comparison of the FUV (SBC) image with the optical (FOC and WFPC2) images; see Figure 1 and also Section 3.2) virtually proves that this object is indeed PSR B1055–52.

Using the offsets between the pulsar counterpart and Star A measured in the SBC image ($2''.02$ and $-3''.92$ in right ascension and declination, respectively), we looked for the pulsar counterpart at the corresponding position in the WFPC2 images. We detected it in both the F702W image (seen in the circle labeled “SBC” in the right panel of Figure 1) and in the F555W image but not in the F450W one.

3.2. Photometry

We measured the magnitudes and fluxes of the PSR B1055–52 counterpart in the WFPC2, ACS/SBC, and FOC images through customized aperture photometry using the IRAF package *digiphot*. For the WFPC2 F555W and F702W bands, we used a small source aperture with the radius $r = 3$ pixels ($0''.135$) to maximize the signal-to-noise ratio (S/N). We sampled the background in a surrounding annulus with the inner radius $r_b = 5$ pixels and radial width $\delta r = 10$ pixels; the distance of 2 pixels from the source aperture was chosen to exclude the brighter portion of the point spread function (PSF)

⁷ Before 2002, the pair of guide stars used to compute the astrometric solution in the *HST* focal plane were selected from the GSC1.0 (Lasker et al. 1990), which had a mean positional error of about $1''.0$. After 2002, the guide stars are selected from the GSC2.3 (Lasker et al. 2008), which has an improved mean positional error of about $0''.3$.

wings. We then applied the aperture correction using the fractional encircled energy (FEE) coefficients (Holtzman et al. 1995), and the correction to compensate for the time- and position-dependent charge transfer efficiency (CTE) losses of the WFPC2 detector (Dolphin 2009). For estimating the 3σ flux upper limit in the F450W band, we used the same $r = 3$ pixels source aperture but sampled the background in a wider annulus, $\delta r = 30$ pixels, around the expected pulsar position.

For the SBC data, we chose a source aperture of $r = 6$ pixels ($0''.2$) and a background annulus with $r_b = 20$ pixels and $\delta r = 10$ pixels. The large radial distance of 14 pixels between the source aperture and the background annulus was chosen to exclude the count excess over the PSF wings, which is seen from the comparison of the count distributions around the pulsar and around Star A (see the insets in the left panel of Figure 1). The 3σ excess (e.g., 114 ± 38 counts in the $0''.3$ – $0''.7$ annulus) cannot be ascribed to different PSFs of the pulsar and Star A because the latter is only one magnitude brighter than the pulsar in the SBC F140LP band, and it is separated from the pulsar by only $4''.41$. From these data alone, we cannot exclude the possibility that the excess is a compact pulsar wind nebula (PWN), but, as the excess is not seen in other bands, it can also be just a small-scale enhancement of the detector background at the pulsar position. Since the brightness profile of Star A is closer to that of the model PSF, we used it as a reference to compute the aperture correction by fitting its growth curve (i.e., the number of source counts within an aperture as a function of its radius).

We also measured anew the magnitude and flux of the counterpart in the FOC image. Following the approach described by Pavlov et al. (1997), we chose an optimal source aperture from the measured growth curves for each of the three orbits. We found that the growth curves for the first and third orbits were consistent with each other and compatible with the nominal values of FEE at $\approx 3400 \text{ \AA}$, while the growth curve for the second orbit showed a peculiar behavior (e.g., no saturation up to $r \sim 20$ pixels, which means an unusually broad PSF). Therefore, we excluded the second orbit data from the analysis and chose $r = 8$ pixels ($0''.11$), $r_b = 10$ pixels, and $\delta r = 10$ pixels.

In all cases, we applied the countrate-to-flux conversion by computing the photometric zero points in the STmag system using the image keywords *PHOTFLAM* and *PHOTZPT*, derived by the *HST* data reduction pipelines. To calculate the extinction-corrected fluxes, we estimated the interstellar reddening toward the pulsar, $E(B - V) = 0.07$, using the hydrogen column density $N_H = 2.7 \times 10^{20} \text{ cm}^{-2}$, derived by De Luca et al. (2005) from the X-ray fits, and using the correlation between N_H and $E(B - V)$ found by Predehl & Schmitt (1995). We then calculated the extinction coefficients using the optical extinction curves by Fitzpatrick (1999) for the WFPC2 and FOC passbands and the UV extinction curves by Seaton (1979) for the SBC passband. The magnitudes and the measured, F_ν^{obs} , and dereddened, F_ν^{der} , spectral fluxes are presented in the last two columns of Table 1.

We plotted the dereddened spectral fluxes F_ν^{der} versus frequency ν in Figure 2. The shape of the broad-

band spectrum and, in particular, the relatively high FUV brightness of the object are inconsistent with it being a non-collapsed star in the Galaxy or an extragalactic object. Therefore, the photometry proves unequivocally that the source is the optical counterpart of PSR B1055–52.

It is clear from Figure 2 that a simple one-component spectral model cannot fit the optical-UV spectral energy distribution (SED). However, similar to the optical-UV spectra of other middle-aged pulsars (e.g., KP07), the SED can be fitted by a model consisting of an (optical) power-law (PL_O) component and a Rayleigh-Jeans (RJ) component:

$$F_{\nu}^{\text{der}} = f_{\text{O}} \left(\frac{\nu}{\nu_0} \right)^{-\alpha_{\text{O}}} + \frac{2\pi}{c^2} \frac{R_{\text{O}}^2}{d^2} kT_{\text{O}} \nu^2, \quad (3)$$

where R_{O} is the radius of equivalent emitting sphere, and T_{O} is the brightness temperature (both as seen by a distant observer). At $E(B - V) = 0.07$, the fitting parameters are $\alpha_{\text{O}} = 1.05 \pm 0.34$, $f_{\text{O}} = 0.112 \pm 0.003 \mu\text{Jy}$ at $\nu_0 = 1 \times 10^{15}$ Hz, and $R_{\text{O}}^2 T_{\text{O}} = (510 \pm 81) d_{750}^2 \text{ km}^2 \text{ MK}$ (or $T_{\text{O}} = (3.02 \pm 0.48) d_{750}^2 R_{\text{O},13}^{-2} \text{ MK}$, where $R_{\text{O},13}$ is the radius in units of 13 km). The PL_O component, which can be interpreted as magnetospheric radiation, dominates in the optical ($\lambda \gtrsim 3000 \text{ \AA}$). The energy flux of this component is $\mathcal{F}_{\text{O}}^{\text{nonth}} \approx 1.3 \times 10^{-15} \text{ erg cm}^{-2} \text{ s}^{-1}$ in the 3000–9000 Å band. The RJ component dominates in the FUV and is likely emitted from the NS surface. We will discuss implications of these results in Section 4.1.

3.3. Astrometry

3.3.1. Absolute position of the pulsar

The pulsar counterpart position given by Equation (2) was obtained from the SBC astrometry using the Star A position in the UCAC3 catalog. Of course, using just one reference star may introduce a significant bias in the absolute target position. Fortunately, the WFPC2 has a much larger FOV than the SBC, allowing astrometry with larger numbers of reference stars.

For the WFPC2 astrometry, we used two catalogs, GSC2.3 (Lasker et al. 2008) and 2MASS (Skrutskie et al. 2006). Although the astrometric accuracy of these catalogs is somewhat lower than that of UCAC3, they contain more stars per given area, which improves the statistics of the astrometric fits. Moreover, most UCAC3 stars identified in the WFPC2 FOV are saturated, which prevents their use for the astrometric calibration. We used the F702W image, in which PSR B1055–52 was detected with a higher S/N than in the F555W image. We produced the WFPC2 mosaic image with the STSDAS task `wmosaic`, which also corrects for the geometric distortion. Then, we measured the centroids of the reference stars (13 stars in GSC2.3 and 16 stars in 2MASS) in the WFPC2 pixel coordinates through gaussian fitting with the Graphical Astronomy and Image Analysis (GAIA) tool⁸ and used the catalog sky coordinates of these stars to compute the pixel-to-sky coordinate transformation with the code `ASTROM`⁹. This yielded astrometric fits with

the rms values $\sigma_r = 0''.17$ for both the GSC2.3 and 2MASS stars. To these we added in quadrature the uncertainties of the registration of the WFPC2 image on the catalog reference frames, $\sigma_{\text{tr}} = 0''.14$ and $0''.08$, for the GSC2.3 and 2MASS, respectively. Following Lattanzi et al. (1997), these uncertainties were estimated as $\sigma_{\text{tr}} = (3/N_{\text{cat}})^{1/2} \sigma_{\text{cat}}$, where $3^{1/2}$ accounts for 3 free parameters in the astrometric fit, σ_{cat} is the mean positional error of the catalog coordinates ($0''.3$ and $0''.2$ for the GSC2.3 and 2MASS, respectively), and N_{cat} is the number of catalog stars used to compute the astrometric solution. Accounting for the $0''.15$ and $0''.015$ uncertainties on the link of the GSC2.3 and 2MASS to the International Celestial Reference Frame (ICRF), the overall uncertainties of the astrometry (1σ position errors) are $\delta_r = 0''.26$ and $0''.19$, respectively.

We applied these astrometric solutions to compute the sky coordinates of PSR B1055–52 from its pixel coordinates. As it has been done for the reference stars, we computed the pixel coordinates through a gaussian fitting, with an uncertainty of $\leq 0''.01$ for the pulsar centroid, negligible in comparison with the overall uncertainty of our absolute astrometry calibration. We then obtained the GSC2.3-based pulsar coordinates

$$\alpha = 10^{\text{h}}57^{\text{m}}58^{\text{s}}961, \quad \delta = -52^{\circ}26'56''.17, \quad (4)$$

with the position error $\delta_r = 0''.26$, and the 2MASS-based coordinates

$$\alpha = 10^{\text{h}}57^{\text{m}}58^{\text{s}}967, \quad \delta = -52^{\circ}26'56''.31, \quad (5)$$

with $\delta_r = 0''.19$. These two positions are consistent with each other and with the UCAC3-based position derived by using Star A as the only reference star in the SBC astrometry (Equation 2).

Since the coordinates in Equations (4) and (5) have been computed using different catalogs and different reference stars, they can be considered independent and hence can be averaged. The calculation of the weighted means yields

$$\alpha = 10^{\text{h}}57^{\text{m}}58^{\text{s}}965, \quad \delta = -52^{\circ}26'56''.26, \quad (6)$$

with $\delta_r = 0''.15$. Thus, the WFPC2 astrometry, recalibrated with the GSC2.3 and 2MASS, has provided the absolute pulsar coordinates at the epoch of 2008.18, which is separated by about 30 years from the epoch of the only published radio position¹⁰.

3.3.2. Proper motion of the pulsar

We used the optical coordinates of PSR B1055–52 to measure its proper motion from the comparison with the radio coordinates at the 1978.13 epoch (Equation 1). We note that, since the GSC2.3 and 2MASS, as well as UCAC3, are linked to the ICRF, there is no a systematic offset between the optical and radio coordinates. Using Equation (6), we infer the displacement $\Delta\alpha \cos \delta = +1''.14 \pm 0''.29$ and $\Delta\delta = +0''.04 \pm 0''.32$, which corresponds to the proper motion

$$\mu_{\alpha} = +38 \pm 10 \text{ mas yr}^{-1}, \quad \mu_{\delta} = +1 \pm 11 \text{ mas yr}^{-1} \quad (7)$$

¹⁰ After completing our astrometric analysis, we became aware that an unpublished radio timing position was recently obtained (R. N. Manchester, private communication), which we found consistent with our own results.

⁸ See star-www.dur.ac.uk/~pdraper/gaia/gaia.html.

⁹ See <http://star-www.rl.ac.uk/Software/software.htm>.

in right ascension and declination. Using the UCAC3-based positions (Equation 2) results in virtually the same proper motion ($\mu_\alpha = 35 \pm 9 \text{ mas yr}^{-1}$, $\mu_\delta = -2 \pm 10 \text{ mas yr}^{-1}$), whose errors are dominated by the errors of the radio position (Equation 1).

The pulsar proper motion can be independently measured through *relative HST* astrometry, by comparing its position with respect to Star A in the SBC image (epoch 2008.12) with that in the FOC image (epoch 1996.36). Of course, measuring a relative proper motion with only one reference star comes with caveats. Firstly, Star A is slightly saturated in the FOC image and part of its PSF is outside the FOC FOV (see Figure 1 of M+97), which lowers the precision of the star centroid determination. To be very conservative, we assumed an uncertainty of 5 pixels ($0''.07$). The pulsar centroids were measured with a much higher precision of $\lesssim 0.1$ pixels in both the SBC and FOC images ($\lesssim 0''.0025$ and $\lesssim 0''.0014$, respectively), and the residual geometric distortion (about $0''.004$ and $0''.007$ rms for the SBC and FOC, respectively – see Apellániz & Cox 2008 and Nota et al. 1996, respectively) is also much smaller than the FOC centroiding uncertainty for Star A.

Secondly, with only one reference star, we have to rely upon the nominal values of the angles between the detector axes and the directions of right ascension and declination, which may introduce an error in the direction of the proper motion. However, this error is very small in our case, thanks to the accuracy of the detector position angle and the small separation of Star A from the pulsar (see § 3.1). Last but not least, the uncertainty of the proper motion of the reference star should be small enough not to hamper the measurement of the relative pulsar proper motion. We carefully verified it for Star A (see Appendix).

Using the value of the pixel scale for the two detectors and the nominal orientations of the two images with respect to the equatorial reference frame, we found the displacement of the pulsar with respect to Star A during the time span of 11.76 years between the two *HST* observations: $\Delta\alpha \cos \delta = 0''.61 \pm 0''.14$ and $\Delta\delta = -0''.19 \pm 0''.14$. The uncertainty of the displacement is dominated by the large uncertainty of the Star A centroid in the FOC image. This displacement corresponds to the proper motion $\mu_\alpha = 52 \pm 6 \text{ mas yr}^{-1}$ and $\mu_\delta = -16 \pm 6 \text{ mas yr}^{-1}$. Correcting these values for the proper motion of star A as given in the UCAC3 catalog (see § 3.1), we obtained

$$\mu_\alpha = 43 \pm 6 \text{ mas yr}^{-1}, \quad \mu_\delta = -5 \pm 6 \text{ mas yr}^{-1}. \quad (8)$$

This proper motion agrees with that measured from the comparison of the radio and optical absolute coordinates. The weighted mean of the proper motion values determined by the two methods is

$$\mu_\alpha = 42 \pm 5 \text{ mas yr}^{-1}, \quad \mu_\delta = -3 \pm 5 \text{ mas yr}^{-1}, \quad (9)$$

or

$$\mu = 42 \pm 5 \text{ mas yr}^{-1}, \quad \text{P.A.} = 94^\circ \pm 7^\circ. \quad (10)$$

for the total proper motion and position angle (counted east of north). The large proper motion provides additional evidence that the M+07 candidate is indeed the pulsar counterpart.

4. DISCUSSION

4.1. Pulsar spectrum

We have shown in Section 3.2 that the optical-UV SED for PSR B1055–52 can be described by a sum of PL_O (magnetospheric) and RJ (thermal) spectra (see Equation 3). It is interesting to compare these optical components with the corresponding spectral components at higher energies, particularly in soft X-rays where both the thermal and magnetospheric components are seen. As we have mentioned in Section 1, the pulsar’s X-ray spectrum can be described by a model that consists of cold BB (BB_C), hot BB (BB_H), and X-ray power-law (PL_X) components. The BB_C and BB_H components are presumably emitted from the bulk of the NS surface and polar caps, respectively, while the PL_X component, $F_\nu = f_X(E/E_0)^{-\alpha_X}$, represents the magnetospheric X-ray emission. The parameters of the three components, as inferred from the *XMM-Newton* data by De Luca et al. (2005), are the following: $T_C = 0.79 \pm 0.03 \text{ MK}$, $R_C = 12.3_{-0.7}^{+1.5} d_{750} \text{ km}$; $T_H = 1.79 \pm 0.06 \text{ MK}$, $R_H = (0.46 \pm 0.06) d_{750} \text{ km}$; and $\alpha_X = 0.7 \pm 0.1$, $f_X = 1.3_{-0.1}^{+0.2} \times 10^{-31} \text{ erg cm}^{-2} \text{ s}^{-1} \text{ Hz}^{-1}$ at $E_0 = 1 \text{ keV}$, respectively. These components and their extrapolations into the optical-UV domain are shown in the left panel of Figure 3.

We see from Figure 3 that the extension of the best-fit PL_X component into the optical overshoots the optical fluxes by a factor of ~ 3 , similar to most of other pulsars detected in the optical (e.g., KP07; Mignani et al. 2010). However, in contrast to the majority of those pulsars, the PL_O component is apparently steeper than the PL_X component ($\alpha_O = 1.05 \pm 0.34$ vs. $\alpha_X = 0.7 \pm 0.1$), and perhaps steeper than the PL_O components in other pulsars (e.g., $\alpha_O = 0.41 \pm 0.08$ and 0.46 ± 0.12 in PSR B0656+14 and Geminga, respectively; see KP07). Moreover, the extrapolation of the best-fit PL_O component into the X-ray range does not intersect the PL_X spectrum, being at least a factor of ~ 10 lower at $E \gtrsim 1 \text{ keV}$. Such behavior is unusual (a notable exception is PSR B0540–69; Mignani et al. 2010), and it might suggest that different populations of ultrarelativistic electrons are responsible for the optical and X-ray emission of PSR B1055–52. However, taking into account the large uncertainties of the spectral slopes, it seems more plausible that α_O is substantially smaller than its best-fit value (e.g., $\alpha_O \lesssim 0.5$), in which case the extrapolation of the PL_O component can, in fact, be smoothly connected with the PL_X spectrum.

Interestingly, the slope $\alpha_\gamma = 0.06 \pm 0.1$ of the *Fermi* LAT spectrum, fit by a PL with an exponential cut-off ($F_\nu \propto E^{-\alpha_\gamma} \exp(-E/E_{\text{cut}})$; Abdo et al. 2010), is even flatter than the X-ray slope. On the other hand, as we see from the right panel of Figure 3, the optical and γ -ray points can be connected by a PL spectrum with the slope $\alpha_{O-\gamma} \approx 0.46$, which, however, goes slightly above the PL tail of the X-ray spectrum. We cannot rule out the possibility that further observations (especially in the IR-optical), supplemented by a joint multiwavelength analysis, will show the magnetospheric spectrum of PSR B1055–52 to be similar to those of other pulsars with optical, X-ray, and γ -ray counterparts, including the other two Musketeers.

Another property of PSR B1055–52 to compare with

those of other pulsars detected in the optical is the relationship between the optical and X-ray luminosities of the magnetospheric emission. For instance, for the wavelength range 4000–9000 Å, the flux in the PL_O component, $\mathcal{F}_O^{\text{nonth}} \approx 0.94 \times 10^{-15} \text{ erg cm}^{-2} \text{ s}^{-1}$, corresponds to the luminosity $L_O^{\text{nonth}} = 4\pi d^2 \mathcal{F}_O^{\text{nonth}} = 6.3 \times 10^{28} d_{750}^2 \text{ erg s}^{-1}$ and optical efficiency $\eta_O \equiv L_O^{\text{nonth}}/\dot{E} = 2.1 \times 10^{-6} d_{750}^2$. At the adopted distance of 750 pc, both the luminosity and efficiency of PSR B1055–52 are considerably higher than those of PSR B0656+14 and Geminga, for which $L_O^{\text{nonth}} = 1.6 \times 10^{28} d_{290}^2$, $\eta_O = 4.2 \times 10^{-7} d_{290}^2$, and $L_O^{\text{nonth}} = 4.8 \times 10^{27} d_{250}^2$, $\eta_O = 1.5 \times 10^{-7} d_{250}^2$, respectively (KP07). This hints that the actual distance to PSR B1055–52 is smaller, which is supported by the analysis of the thermal emission below. On the other hand, the ratio of the optical (4000–9000 Å) and X-ray (1–10 keV) nonthermal luminosities, $L_O^{\text{nonth}}/L_X^{\text{nonth}} = 0.9 \times 10^{-2}$ (which does not depend on the distance), is within the same range of $\sim 10^{-3}$ – 10^{-2} as for all other pulsars with optical counterparts (Zavlin & Pavlov 2004; Zharikov et al. 2006).

Let us now compare the optical-UV and X-ray *thermal* components of the PSR B1055–52 spectrum. The BB_H component is not seen in the optical because of the small emitting area, while the extrapolation of the BB_C into the optical-UV is a factor of ≈ 4 below the observed RJ component. Such an “optical-UV excess” of the RJ component has been seen in the nearby radio-quiet isolated NSs (RQINSs), such as RX J1856.5–3754 and RX J0720.4–3125 (e.g., Kaplan 2008, and references therein), and in the millisecond pulsar J0437–4715 (Kargaltsev et al. 2004). It, however, has not been observed in middle-aged pulsars. In particular, the extrapolated BB_C component lies slightly *above* the optical-UV RJ component in Geminga (Kargaltsev et al. 2005), while these components virtually coincide with each other in PSR B0656+14 (KP07).

The nature of the optical-UV excess is not fully understood; a popular hypothesis is that it is due to a nonuniform distribution of the temperature over the NS surface, such that the BB_C component originates from a smaller and hotter region than the optical-UV RJ component (e.g., Pavlov et al. 2002). Such an assumption is crudely equivalent to adding a “very cold” thermal component, BB_{VC}, which dominates in the UV but makes very little contribution in X-rays. In other words, the product $R_O^2 T_O$ in the second term of Equation (3) is approximately equal to $R_C^2 T_C + R_{VC}^2 T_{VC}$. Taking into account that $R_C^2 T_C \approx 119 d_{750}^2 \text{ km}^2 \text{ MK}$ and $R_O^2 T_O \approx 510 d_{750}^2 \text{ km}^2 \text{ MK}$, we obtain $R_{VC}^2 T_{VC} \approx 391 d_{750}^2 \text{ km}^2 \text{ MK}$ (or $T_{VC} \approx 2.31 d_{750}^2 R_{VC,13}^{-2} \text{ MK}$). Unfortunately, we cannot measure T_{VC} independent of d^2/R_{VC}^2 in the RJ regime. We can, however, estimate an upper limit on T_{VC} from the requirement that the BB_{VC} spectral flux extrapolated to soft X-ray energies becomes so small, in comparison with the BB_C, that it does not affect the X-ray fit. We found that it occurs at $T_{VC} \lesssim 0.45 \text{ MK}$ (at this temperature the contribution of the BB_{VC} flux is $\lesssim 10\%$ above 0.3 keV – see Figure 3, left).

Such a limit on T_{VC} implies a considerably smaller distance to the pulsar than that estimated from the pulsar’s

dispersion measure. Indeed, from the above estimate on $R_{VC}^2 T_{VC}$ we obtain $d \lesssim 25.4 (R_{VC}/1 \text{ km}) \text{ pc} < 330 R_{NS,13} \text{ pc}$, where we took into account that R_{VC} is smaller than the NS radius, $R_{NS} = 13 R_{NS,13} \text{ km}$. Since the NS radius (as seen from infinity) can hardly exceed 20 km, the distance is $< 500 \text{ pc}$, and it can even be substantially smaller than this upper limit.

We should note that such estimates are, of course, model dependent. For instance, the temperature distribution over the NS surface can be smooth (i.e., there are no three distinct regions as we implicitly assumed above). Moreover, the spectrum of the thermal emission from a NS surface region can differ from the BB, which may lead to an excess of the actually emitted optical-UV thermal component over the extrapolation of the X-ray thermal component even if the surface temperature is uniform (e.g., in the case of a light-element, H or He, NS atmosphere; Pavlov et al. 1996). However, fitting the model light-element atmosphere spectra to the observed X-ray spectrum always leads to a lower temperature and a larger value of R/d (i.e., to a smaller distance at a given NS radius) than those obtained from the BB fits (Pavlov et al. 1995). Therefore, it seems hard to avoid the conclusion on a smaller distance¹¹, although its value cannot be determined accurately from the data available. We believe 200 pc and 500 pc are reasonable lower and upper limits, and we will scale the distance to 350 pc below.

The conclusion that the distance is smaller than previously thought has important implications. For instance, the radius of the BB_C emitting region, $R_C = 5.7_{-0.3}^{+0.7} d_{350} \text{ km}$, becomes substantially smaller than a plausible NS radius. It means that $T_C = 0.79 \pm 0.03 \text{ MK}$ is *not* the temperature of the entire NS surface, and it should *not* be used for comparisons with the NS cooling models. This removes the problem of PSR B1055–52 being too hot and luminous ($L_{C,\text{bol}} = 4.2 \times 10^{32} d_{750}^2 \text{ erg s}^{-1}$) for its age, in comparison with other middle-aged NSs and the predictions of standard NS cooling models (e.g., Yakovlev & Pethick 2004). It also means that PSR B1055–52 is not a “very slowly cooling NS” (as suggested by Kaminker et al. 2002), and there is no need to invoke an unusually low NS mass to explain its thermal emission (see Yakovlev & Pethick 2004 for references). To infer the true thermal luminosity and average surface temperature, and compare them with the predictions of the NS cooling models, the parallax-based distance to the pulsar should be measured, and the distribution of the temperature over the NS surface should be determined from the phase-resolved spectral analysis of the pulsar’s soft X-ray and FUV emission.

Another implication of the smaller distance is that the magnetospheric luminosities and efficiencies in various spectral bands are lower than previously thought, being close to the luminosities and efficiencies of other pulsars. For instance, if $d \sim 350 \text{ pc}$, its γ -ray efficiency, $\eta_\gamma \sim 0.13 d_{350}^2$ in the 0.1–100 GeV band (Abdo et al. 2010),

¹¹ Note a similar discrepancy between the DM-based distance estimate (750 pc, in the model by Taylor & Cordes 1993) and the distance determined from parallax measurements ($288_{-27}^{+33} \text{ pc}$; Briskin et al. 2003) for PSR B0656+14. Interestingly, Anderson et al. (1993) estimated the distance to be $280_{-50}^{+60} \text{ pc}$ using the NS atmosphere models by Shibano et al. (1993) and ROSAT data.

although still rather high, becomes not so different from the efficiencies of other pulsars detected with *Fermi* LAT, and the optical efficiency, $\eta_{\text{O}} = 4.6 \times 10^{-7} d_{350}^2$, becomes comparable with those of PSR B0656+14 and Geminga.

4.2. Pulsar astrometry and kinematics

PSR B1055–52 is the third rotation-powered pulsar, after Geminga (Caraveo et al. 1998) and PSR B0540–69 (Mignani et al. 2010), for which an absolute position has been determined with a sub-arcsecond accuracy using optical astrometry techniques. Knowing the astrometric position will be useful for the precise timing analysis of the pulsar.

The proper motion we measured for the pulsar’s optical counterpart (Equation 11) corresponds to a tangential velocity $V_t = (70 \pm 8) d_{350} \text{ km s}^{-1}$. This value is well below the average 400 km s^{-1} for radio pulsars (Hobbs et al. 2005), but it is close to that of the Vela pulsar ($V_t \sim 65 \text{ km s}^{-1}$; Caraveo et al. 2001).

The proper motion in Galactic coordinates,

$$\mu_l = 39 \pm 5 \text{ mas yr}^{-1}, \quad \mu_b = 15 \pm 5 \text{ mas yr}^{-1}, \quad (11)$$

shows that the pulsar, whose current coordinates are $l = 285.984^\circ$ and $b = +6.649^\circ$, is moving away from the Galactic plane. We attempted to use the proper motion to locate the pulsar’s birth place, identify a parent star cluster (OB association), and estimate the actual age of the pulsar that can differ from its spin-down age. However, to calculate the pulsar’s trajectory back in time in the Galactic potential, one should know the present distance (which is poorly known), the tangential velocity (proportional to the distance), and the radial velocity V_r (which is unknown). Therefore, one has to calculate a large set of pulsar trajectories for various values of d and V_r . Using the code developed by Vande Putte et al. (2010), we calculated the trajectories on a grid of 21 distances (in the range of 200 to 1200 pc) and 21 radial velocities (-500 to $+500 \text{ km s}^{-1}$). We also selected a sample of young ($< 100 \text{ Myr}$) clusters/associations (de Zeeuw et al. 1999; Dias et al. 2002) in a 25° radius circle around the present position of the pulsar, extrapolated back in time their motion using the same code, and looked for closest approaches of the pulsar and cluster trajectories. The results, however, turned out to be rather ambiguous because different values of d and (especially) V_r resulted in quite different candidate parent associations and pulsar ages (e.g., we found 10 candidates for the age range of 400–700 kyr), and the uncertainty of \mathbf{V}_t propagated back in time resulted in very large uncertainties on the minimum separations. These uncertainties becomes even larger if one also accounts for the errors on the cluster proper motions, distances, and radial velocities. To obtain a more certain solution, we have to wait for the measurement of the pulsar’s parallax and more accurate measurements of the proper motion, together with observational constraints on the pulsar’s radial velocity, which could come, e.g. from the modelling of a possible bow-shock PWN created in the ISM by the supersonically moving pulsar (see, e.g. Pellizza et al. 2005).

5. SUMMARY

Using the *HST* observations, we have confirmed that the candidate proposed by M+97 is indeed the optical-UV counterpart of PSR B1055–52, the tenth rotation-powered pulsar with a secured optical identification (see Mignani 2010 for a recent review). From multi-band photometry we found that, similar to the middle-aged pulsars PSR B0656+14 and Geminga, its spectrum can be described by the combination of a PL_{O} component, with the spectral index $\alpha_{\text{O}} = 1.05 \pm 0.34$, and a RJ component, with brightness temperature $T_{\text{O}} = (0.66 \pm 0.10) d_{350}^2 R_{\text{O},13}^{-2} \text{ MK}$. The PL_{O} component is steeper than those of PSR B0656+14 and Geminga and, possibly, of all the other rotation-powered pulsars with known optical counterparts. Moreover, it is possibly steeper than the X-ray PL component, which might suggest that different populations of relativistic electrons are responsible for the X-ray and optical-UV magnetospheric emission. To verify this assumption, IR observations of PSR B1055–52 would be particularly useful, supplemented by a joint spectral fit of the IR-optical, X-ray, and γ -ray components, using multiwavelength spectral models for magnetospheric pulsar emission.

The observed RJ component exceeds by a factor of ≈ 4 the extrapolation of the X-ray thermal component into the UV-optical, unlike PSR B0656+14 and Geminga but similar to RQINSs. It indicates that the temperature distribution over the NS surface is nonuniform, and the X-ray thermal component comes from a relatively small hotter region, while the main contribution to the optical-UV RJ component comes from a larger and colder area. It implies that the distance to the pulsar is considerably smaller than estimated from the pulsar’s dispersion measure and the models for Galactic electron distribution. It also means that the conclusions inferred from the comparison of the X-ray temperature and thermal luminosity of PSR B1055–52 with the NS cooling models require a revision. New *HST* observations in the UV and near-IR, including phase-resolved spectroscopy, are required to separate the thermal and magnetospheric components and infer the temperature distribution, while the measurement of the radio parallax is crucial to determine the actual distance and the NS radius.

By recalibrating the astrometry of the *HST* images with the GSC2.3, 2MASS and UCAC3 catalogs, we have measured the PSR B1055–52 absolute coordinates with a radial position accuracy of $0''.15$ at the epoch of 2008.18, about 30 years after the measurement of the only published pulsar’s coordinates. From relative astrometry between the *HST* images taken 12 years apart, we obtained the first measurement of the pulsar’s proper motion, $\mu = 42 \pm 5 \text{ mas yr}^{-1}$ with a position angle of $94^\circ \pm 7^\circ$, which corresponds to the transverse velocity $V_t = (70 \pm 8) d_{350} \text{ km s}^{-1}$. Further *HST* and radio observations will allow one to measure the proper motion with a higher accuracy, to determine the distance from the parallax measurement, and find the true pulsar age and the parent cluster/association.

Support for Program number 11154 was provided by NASA through a grant from the Space Telescope Science Institute, which is operated by the Association of Universities for Research in Astronomy, Incorporated, under NASA contract NAS5-26555. RPM thanks A. C. Jackson

for her contribution in the reduction of the VLT data. We thank R. N. Manchester for communicating the radio timing position of PSR B1055–52 before publication, A. Dolphin for useful discussions of the corrections for CTE losses in WFPC2, D. Vande Putte for making available to us his code for Galactic orbit simulations, and M. van Kerkwijk for his valuable advice on the search for the

pulsar’s birthplace. We also thank the anonymous referee for the very careful reading of the manuscript and the useful suggestions that helped us to improve the presentation of the results. The work by GGP and OK was partially supported by NASA grant NNX09AC84G.

Facilities: HST (ACS, WFPC2), VLT (FORs1)

APPENDIX

STAR A PROPER MOTION

Since the magnitude of the Star A proper motion is crucial for determining the pulsar’s absolute position and proper motion (see Sections 3.1 and 3.3.1), we verified the UCAC3 value ($\mu_\alpha = -8.9 \pm 1.3$ mas yr⁻¹; $\mu_\delta = 7.8 \pm 2.2$ mas yr⁻¹) against other astrometric catalogs. Unfortunately, star A is too faint ($V \approx 14.6$) to be in the Hipparcos catalog ($V < 12.4$; Perryman et al. 1997), while it is strangely not in the deeper Tycho-2 ($V < 15.2$; Høg et al. 2000) and UCAC2 ($R < 16$; Zacharias et al. 2004). It is, however, in the USNO-B1.0 catalog ($B < 22$; Monet et al. 2003), which reports a proper motion of $\mu_\alpha = +30 \pm 4$ mas yr⁻¹ and $\mu_\delta = 0 \pm 6$ mas yr⁻¹ (much larger than in UCAC3), and in the PPMXL catalog (Roeser et al. 2010), which gives $\mu_\alpha = -13.8 \pm 8.2$ mas yr⁻¹ and $\mu_\delta = +4.5 \pm 8.2$ mas yr⁻¹, consistent with the UCAC3 value (albeit less accurate).

As an independent test, we measured the relative proper motion of Star A. We used archival Very Large Telescope (VLT) images of the PSR B1055–52 field taken with FOCAL Reducer/low dispersion Spectrograph (FORs1) on 2002 March 21, which yields a time baseline of about 6 years with respect to the WFPC2 observations. The images were taken in high resolution mode (0’1/pixel) but with a windowing of the CCD (1’6 × 1’6 FOV). A sequence of eighteen 140 s dithered exposures was obtained through the Bessel B filter ($\lambda = 4290 \text{ \AA}$; $\Delta\lambda = 880 \text{ \AA}$). We applied standard CCD reduction with the MIDAS package and performed the astrometric calibration as described in Section 3.3 (position error $\delta_r = 0’3$). Unfortunately, the image quality of the FORs1 data (seeing $\sim 1’2$) does not allow one to detect the pulsar in the halo of Star A.

We then compared the relative position of Star A measured in the FORs1 (2002.21) and WFPC2 (2008.18) images. We used the F450W WFPC2 image, where Star A is not saturated and the pivot wavelength is similar to that of the Bessel B filter. We registered the WFPC2 image onto the FORs1 image, aligned along right ascension and declination to better than $\sim 0.05^\circ$, by computing the transformation between the pixel coordinates of 15 stars seen in both images. This yielded an rms of 0’015 along each of the two axes, larger than the object centroid uncertainty (0’003). We thus determined the offset of Star A to be $\Delta\alpha \cos\delta = -2.2 \pm 15$ mas and $\Delta\delta = 24.6 \pm 15$ mas, which corresponds to the 3σ upper limit on the proper motion of ~ 15 mas yr⁻¹, consistent with both the UCAC3 and PPMXL values.

REFERENCES

- Abdo, A. A., et al. 2010, ApJS, 187, 460
 Anderson, S. B., Córdoba, F. A., Pavlov, G. G., Robinson, C. R., & Thompson, R. J., Jr. 1993, ApJ, 414, 867
 Apellániz, J. M., & Cox, C. 2008, A New Geometric Distortion Solution for the ACS/SBC, Instr. Science Rep. ACS 2008-2, Space Telescope Science Institute
 Becker, W., & Trümper, J. 1997, A&A, 326, 682
 Bignami, G. F., Caraveo, P. A., & Vacanti, G. 1988, A&A, 196, 191
 Brisken, W. F., Thorsett, S. E., Golden, A., & Goss, W. M. 2003, ApJ, 593, L98
 Brinkmann, W. & Ögelman, H. 1987, A&A, 182, 71
 Caraveo, P. A., Lattanzi, M. G., Massone, G., Mignani, R. P., Makarov, V. V., Perryman, M. A. C., Bignami, G. F. 1998, A&A, 329, L1
 Caraveo, P. A., De Luca, A., Mignani, R. P. & Bignami, G. F. 2001, ApJ, 561, 930
 Cheng, A. F., & Helfand, D. J. 1983, ApJ, 271, 271
 Cordes, J. M., & Lazio, T. J. W. 2002, preprint (astro-ph/0207156)
 De Luca, A., Caraveo, P. A., Mereghetti, S., Negroni, M., Bignami, G. F. 2005, ApJ, 623, 1051
 de Zeeuw, P. T., Hoogerwerf, R., de Bruijne, J. H. J., Brown, A. C. A., & Blaauw, A. 1999, AJ, 117, 354
 Dias, W. S., Alessi, B. S., Moitinho, A., & Lépine, J. R. D. 2002, A&A, 389, 871
 Dolphin, A. E., 2009 PASP, 121, 655
 Fierro, J. M., et al. 1993, ApJ, 413, L27
 Fitzpatrick, E. L., 1999, PASP, 111, 63
 Greiveldinger, C., et al. 1996, ApJ, 465, L35
 Guillemot, L. 2009, in Fermi Symposium 2009, on-line talks
 Hobbs, G., Lorimer, D. R., Lyne, A. G., & Kramer, M. 2005, MNRAS, 360, 974
 Høg, E., et al. 2000, A&A, 355, L27
 Kaminker, A. D., Yakovlev, D. G., & Gnedin, O. Y. 2002, A&A, 383, 1076
 Kaplan, D. L. 2008, Proc. of 40 Years of Pulsars: Millisecond Pulsars, Magnetars and More, AIP Conf. Proc., 983, 331
 Kargaltsev, O., Pavlov, G. G., & Romani, R. W. 2004, ApJ, 602, 327
 Kargaltsev, O., Pavlov, G. G., Zavlin, V. E., & Romani, R. W. 2005, ApJ, 625, 307
 Kargaltsev, O. & Pavlov, G. G. 2007, Ap&SS, 308, 287 (KP07)
 Lasker, B. M., Sturch, C. R., McLean, B. J., Russel, J. L., Jenkner, H., & Shara, M. M. 1990, AJ, 99, 2019
 Lasker, B. M., et al. 2008, AJ, 136, 735
 Lattanzi, M. G., Capetti, A., & Macchetto, F. D. 1997, A&A, 318, 997
 Manchester, R. N., et al. 1978, MNRAS, 184, 159
 Manchester, R. N., Hobbs, G. B., Teoh, A., & Hobbs, M. 2005, AJ, 129, 1993
 Mignani, R., Caraveo, P. A., & Bignami, G. F. 1997, ApJ, 474, L51 (M+97)
 Mignani, R. P., Zharikov, S., & Caraveo, P. A. 2007, A&A, 473, 891
 Mignani, R. P., Sartori, A., De Luca, A., Rudack, B., Słowikowska, A., Kanbach, G., Caraveo, P. A. 2010, A&A, 515, 110
 Mignani, R. P. 2010, ASpR, in press (arXiv:0912.2931)
 Mineo, T., Massaro, E., Cusumano, G., & Becker, W. 2002, A&A, 392, 181
 Monet, D. G., et al. 2003, AJ, 125, 984

- Newton, L. M., Manchester, R. N., & Cooke, D. J. 1981, MNRAS, 194, 841
- Nota, A., et al., 1996, FOC Instrument Handbook Ver. 7.0 (Baltimore: STScI)
- Ögelman, H., & Finley, J.P. 1993, ApJ, 413, L31
- Pavlov, G. G., Shibano, Yu. A., Zavlin, V. E., & Meyer, R. D. 1995, in *The Lives of the Neutron Stars*, eds. M. A. Alpar, U. Kiziloglu, & J. van Paradijs (Kluwer: Dordrecht), p.71
- Pavlov, G. G., Zavlin, V. E., Trümper, J., & Neuhäuser, R. 1996, ApJ, 472, L33
- Pavlov, G. G., Welty, A. D., & Córdoba, F. A. 1997, ApJ, 489, L75
- Pavlov, G. G., Zavlin, V. E., & Sanwal, D. 2002, in *Neutron Stars, Pulsars and Supernova Remnants*, eds. W. Becker, H. Lesch, & J. Trümper, MPE-Report 278, 273 (astro-ph/0206024)
- Pellizza, L. J., Mignani, R. P., Grenier, I. A., & Mirabel, I. F. 2005, A&A, 435, 625
- Perryman M. A. C., et al. 1997, A&A, 323, L49
- Predehl, P., & Schmitt, J. H. M. M. 1995, A&A, 293, 889
- Roeser, S., Demleitner, M., & Schilbach, E. 2010, AJ, 139, 2440
- Seaton, M.J. 1979, MNRAS, 187, 73
- Shibanov, Yu. A., Zavlin, V. E., Pavlov, G. G., & Ventura, J. 1993, A&A, 266, 313
- Skrutskie, M. F., et al. 2006, AJ, 131, 1163
- Taylor, J. H., & Cordes, J. M. 1993, ApJ, 411, 674
- Thompson, D. J., et al. 1999, ApJ, 516, 297
- Vande Putte, D. W., Garnier, T. P., Ferreras, I., Mignani, R. P., & Cropper, M. S. 2010, MNRAS, in press
- Vaughan, A. E. & Large, M. L. 1972, MNRAS, 156, 27P
- Weltevred, P., et al., 2010, PASA, 27, 64
- Yakovlev, D. G., & Pethick, C. J. 2004, ARA&A, 42,169
- Zacharias, N., et al. 2004, AJ,127, 3043
- Zacharias, N., et al. 2010, AJ, 139, 2184
- Zavlin, V. E., & Pavlov, G. G. 2004, ApJ, 616, 452
- Zharikov, S., Shibano, Yu., Komarova, V. 2006, AdSpR, 37, 1979

TABLE 1
HST PHOTOMETRY OF THE PSR B1055–52 COUNTERPART.

Filter	$\log \nu$ [Hz]	t s	r pix	C_r^a counts	m_r	Δm_r	Δm_{CTE}	m_{obs}	F_ν^{obs} μJy	F_ν^{der} μJy
WFPC2 F450W	14.818 (0.045)	600	3	<13.7	>25.61	-0.27	-0.37	>24.97	< 0.26	< 0.34
WFPC2 F555W	14.741 (0.049)	600	3	27.3 ± 5.0	25.90 ± 0.20	-0.24	-0.23	25.43	0.241 ± 0.044	0.295
WFPC2 F702W	14.637 (0.043)	600	3	30.3 ± 3.5	26.46 ± 0.13	-0.26	-0.13	26.08	0.214 ± 0.024	0.249
SBC F140LP	15.293 (0.042)	5569	6	525 ± 24	22.83 ± 0.05	-0.19	...	22.64	0.248 ± 0.011	0.417
FOC F342W	14.945 (0.033)	2916	8	242 ± 13	25.18 ± 0.06	-0.18	...	25.00	0.140 ± 0.008	0.190

NOTE. — Columns report the camera and the filter, the pivot frequency and the band width (in parentheses) in logarithmic units (as derived from the SYNPHOT tables), the integration time of the average-combined frames, the photometry aperture radius r in detector pixels, the total number of counts (C_r) measured within the aperture r , the corresponding magnitude in the STmag system (m_r), the aperture correction (Δm_r), the CTE correction (Δm_{CTE}), the observed magnitude m_{obs} , and the observed (F_ν^{obs}) and extinction-corrected (F_ν^{der}) spectral fluxes.

^aFor the WFPC2 and FOC observations, counts have been measured on the average-combined frames. For the FOC, we used only the average of the first and second exposure (see § 3.2).

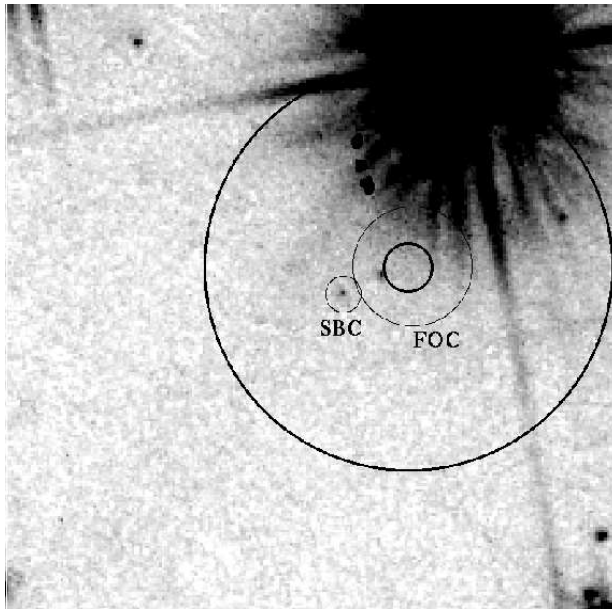


FIG. 1.— SBC F140LP (FUV band; left panel) and WFPC2 F702W (red band; right panel) images of the PSR B1055–52 field ($10'' \times 10''$). North is to the top, East to the left. The two objects in the SBC image are the pulsar (in the smaller thin circle of $0''.3$ radius, corresponding to a nominal uncertainty of SBC position) and Star A ($4''.4$ northwest of the pulsar). Zoomed images of the pulsar and Star A, demonstrating the count distributions in and around these sources, are shown in the insets; the radii of the circles in the insets are $0''.3$ and $0''.7$. The small thin circle in the WFPC2 panel, labeled “SBC” is at the same position with respect to Star A as in the left (SBC) panel. In each of the panels the smaller thick circle of $0''.45$ radius is the error circle around the radio pulsar position at the epoch of 1978.13 (Newton et al. 1981), while the larger thick circle of $3''.4$ radius encloses possible positions of the pulsar at the epoch of our *HST* observations if the pulsar transverse velocity (in an unknown direction) were 400 km s^{-1} , at $d = 750 \text{ pc}$. The thin circle labelled “FOC” corresponds to the position of the PSR B1055–52 candidate counterpart of M+97; its radius of $1''.0$ corresponds to the uncertainty of a nominal FOC position. See § 3.1 for more detail. Notice the much higher relative brightness of the pulsar in the SBC image.

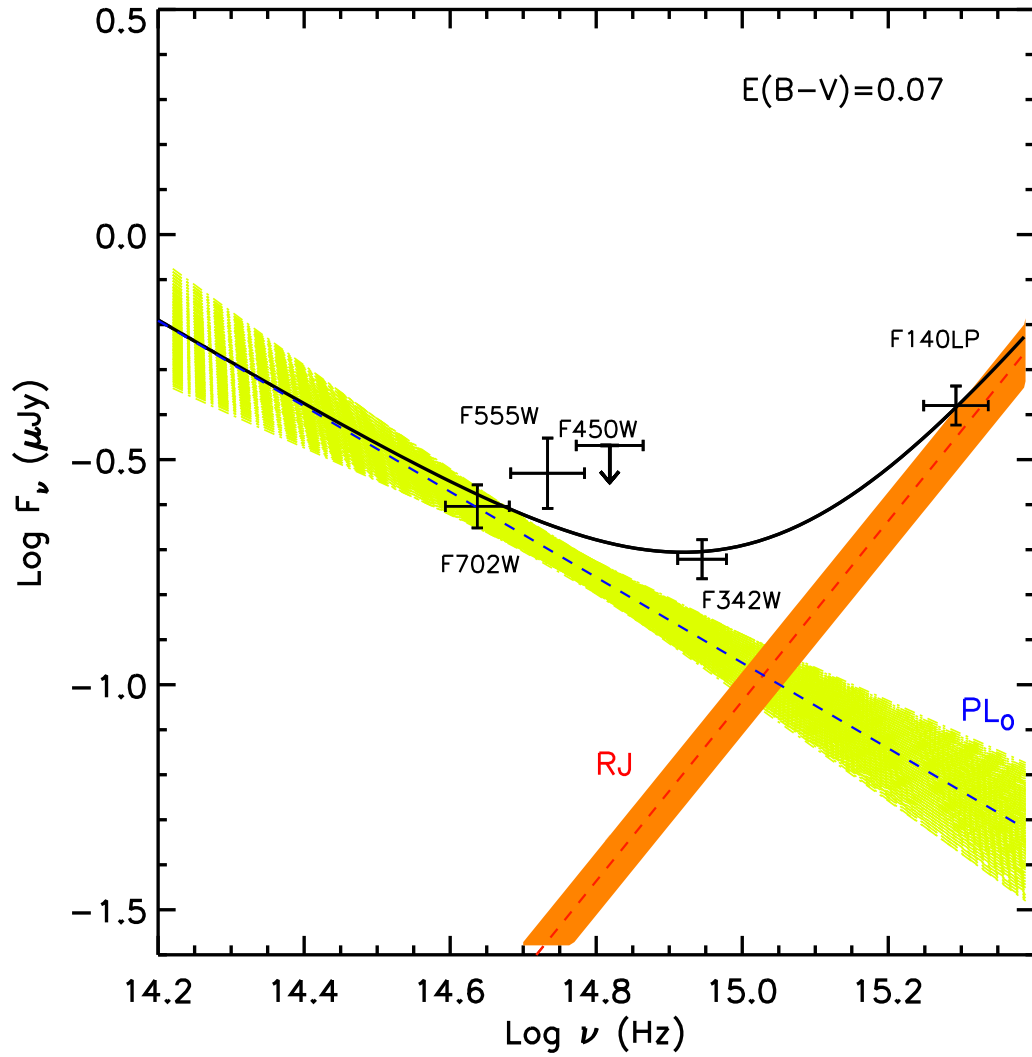


FIG. 2.— Optical-UV spectrum of PSR B1055-52. The spectral fluxes have been corrected for interstellar extinction assuming $E(B-V) = 0.07$. The dashed lines correspond to the Rayleigh-Jeans (RJ; red) and power-law (PL₀; blue) components of the best fit, the solid line shows the sum of these components. The shaded areas show 1σ uncertainties of the fit.

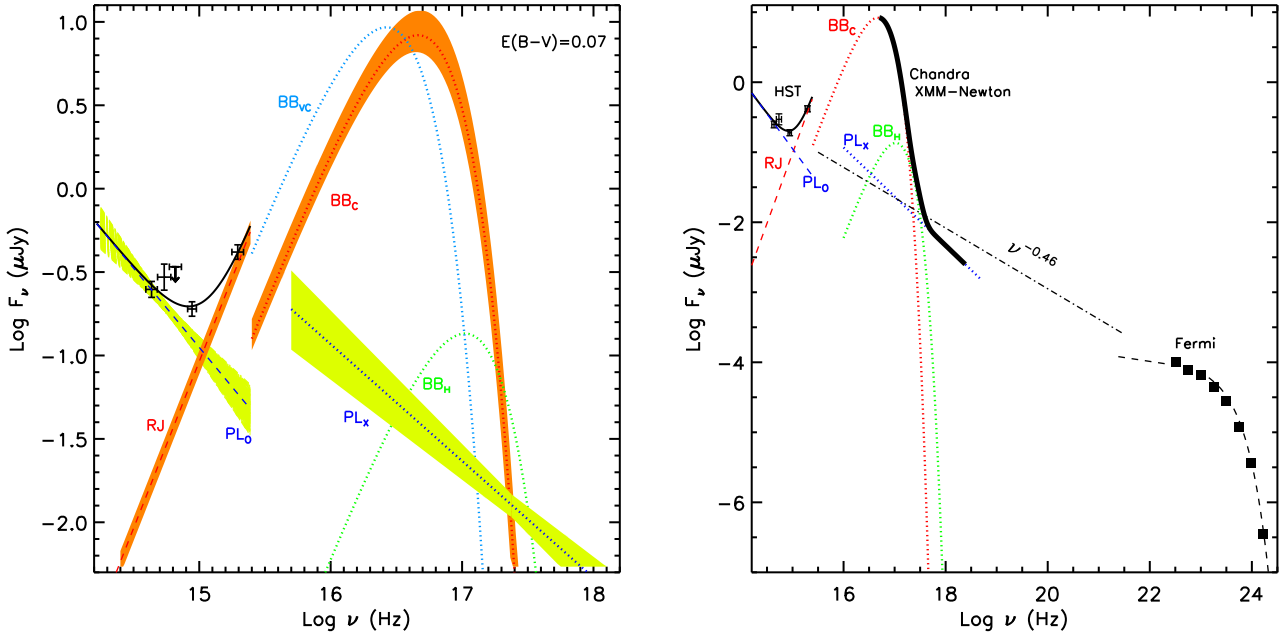


FIG. 3.— *Left*: Comparison of the optical-UV and X-ray spectral models for PSR B1055–52. The X-ray fit for the $\text{BB}_{\text{C}} + \text{BB}_{\text{H}} + \text{PL}_{\text{X}}$ model is taken from De Luca et al. (2005). The excess of the RJ component over the extrapolation of the X-ray BB_{C} component into the optical-UV range could be explained by the presence of a “very cold” thermal component, BB_{VC} . The dotted blue curve shows this component for the maximum allowed temperature $T_{\text{VC}} = 0.45$ MK. The shaded areas show 1σ uncertainties of the fits. *Right*: Multiwavelength SED for PSR B1055–52, from optical to γ -rays, with spectral models for separate ranges. The γ -ray points are from Guillemot (2009), the spectral model from Abdo et al. (2010). The line $\nu^{-0.46}$ shows a PL spectrum approximately connecting the optical and γ -ray bands. See Section 4.1 for more details.